

Development of Interdigitated Array Electrodes with Surface-enhanced Raman Scattering Functionality

Md. Monirul ISLAM,* Kosei UENO,*,** Saulius JUODKAZIS,* Yukie YOKOTA,* and Hiroaki MISAWA*†

*Research Institute for Electronic Science, Hokkaido University, Sapporo 001-0021, Japan

**PRESTO, Japan Science and Technology Agency, Kawaguchi 332-0012, Japan

Interdigitated array electrodes with surface-enhanced Raman scattering (SERS) functionality for *in situ* qualitative and quantitative analysis of electroactive species are demonstrated. Gold nanostructured interdigitated array electrodes (NIDAEs) were fabricated by electron beam lithography, and used for an electrochemical SERS study of $K_3[Fe(CN)_6]$ in aqueous $KClO_4$ solution in single and generation-collection modes. The generation-collection mode experiment showed amplification of the SERS band intensity for adsorbed ferricyanide ions at the negative end of the applied potential, while in single mode it was reduced to near zero. This new finding reveals that NIDAEs offer a new opportunity for analytical science by improving analytical sensitivity and detection ability of electroactive species. The electric fields accumulating at nanogaps are promising for manipulating linear and nonlinear optical phenomena. In addition, miniaturized NIDAEs are of great importance for developing lab-on-a-chip devices, and are useful for measurements within small space/volume domains, requiring only small amounts and/or concentrations of analytes.

(Received October 27, 2009; Accepted November 13, 2009; Published January 10, 2010)

Introduction

Among various microelectrodes and their arrays, interdigitated array electrodes (IDAEs) are well recognized among analytical scientists¹⁻⁵ and have been exploited in several applications such as detectors for lab-on-a-chip systems,⁶⁻¹⁰ scanning electrochemical microscopes (SECM),¹¹ quantitative trace analyzers of redox species,¹² nanoparticle detection devices,¹³ analytical and bioanalytical sensors and others due to their high current amplification characteristics achieved by redox cycling or feedback effects.¹⁴⁻¹⁶ However, electrochemical methods are not fruitful for analyzing the mixtures of electroactive species because of the additive diffusion fluxes of the components.¹⁷ In addition, these techniques can rarely detect short-lived transients and predict their molecular structures. The investigation of the potential-induced structural changes, and the simultaneous qualitative and quantitative analyses even for mixtures require the integration of these techniques with vibrational spectroscopy.¹⁸

The surface-enhanced Raman scattering¹⁹ (SERS) spectroscopy is widely used for gaining mechanistic and dynamic information on the electrode interfaces,²⁰⁻²² amplification of very weak signals generated from single molecules or from ultra short-lived transient species, single molecule detection and trace analysis. Several available reports^{23,24} on electrochemical SERS studies indicated more or less success because of non-reproducible SERS signals caused by surface inhomogeneity. To the best of our knowledge, electrochemical SERS studies with microelectrodes have not hitherto been reported. Microelectrodes with SERS functionality are of great importance for the development of miniaturized systems. Nanostructured

interdigitated array electrodes (IDAEs) with SERS functionality are particularly promising in the field of analytical science. The generation-collection (GC) mode experiment associated with IDAEs accumulates the electroactive species to the electrode surface through the redox cycling or feedback effects, and amplifies the redox current. As the redox cycling mechanism proliferate the concentration of redox entities at or close to the electrode surface, it can amplify the SERS signals, and hence could improve the sensitivity of analytical methods and allow performing the simultaneous quantitative and qualitative analyses with greater sensitivity.

In this article, a gold nanostructured interdigitated array electrode (NIDAE) with high SERS functionality was demonstrated as a new analytical tool. NIDAEs are fabricated by electron beam lithography (EBL) and lift-off techniques with nanopattern definition down to nanometer resolution of the gap sizes for SERS function. A proof-of-principle demonstration of the SERS-active NIDAE capabilities is achieved by electrochemical SERS responses using reversible electroactive species of 10^{-3} mol dm^{-3} aqueous $K_3[Fe(CN)_6]$ including 0.05 mol dm^{-3} $KClO_4$.

Experimental

Fabrication of electrodes

NIDAEs were fabricated on glass substrates (24×24 -mm-square and 0.5-mm-thick; from Matsunami, Ltd.) using high-resolution EBL, UV photolithography, ultra-high vacuum sputtering and lift-off, as reported elsewhere.²⁵⁻²⁷

A conventional co-polymer positive tone resist (ZEP-520A, Zeon Co., Ltd., Tokyo, Japan) for EBL diluted with ZEP thinner (1:1) was spin-coated on the glass substrate and then baked on a hot plate at $180^\circ C$ for 2 min. Patterns of NIDAE were transferred onto substrates by exposing the resist to an electron beam (beam current 5 pA) at 100 kV (ELS-7700H, Elionix Co., Ltd., Tokyo, Japan), and subsequently developing them in

† To whom correspondence should be addressed.

E-mail: misawa@es.hokudai.ac.jp

S. J. present address: Centre for Micro-Photonics, Swinburne University of Technology, Hawthorn VIC 3122, Australia.

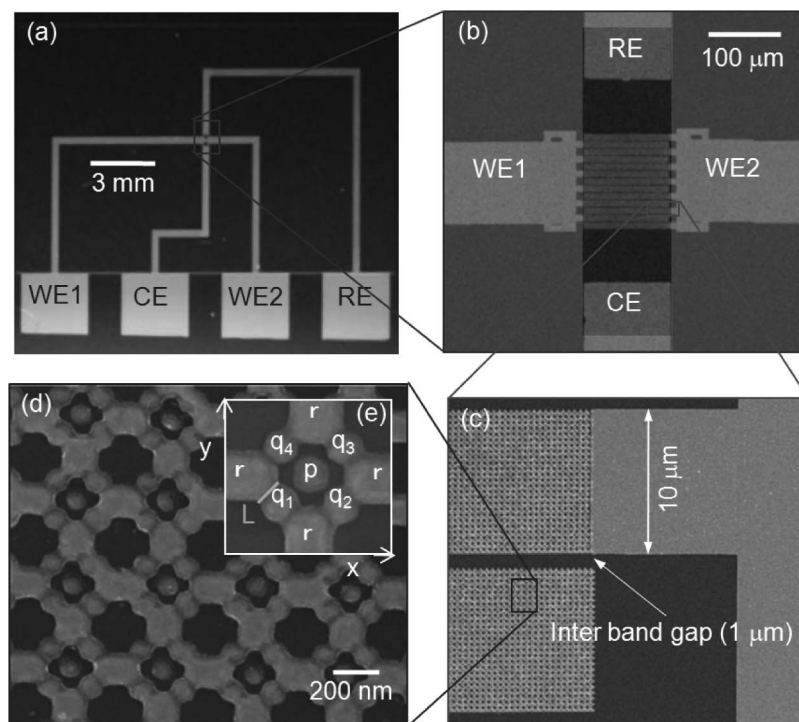


Fig. 1 Schematic representation of NIDAEs, RE, CE and WE refer to reference, counter and working Au electrodes. (a) Optical image; (b) - (e) SEM images at different magnifications. The yellow film in (b) over the surface indicates a passivation film. (e) illustrates the construction of base unit: x , horizontal axis; y , vertical; z , perpendicular to both x - and y -axes; $dx = dy = 400$ nm, for L , p , q_i and r see text in details.

ZEP-N50 (*n*-amyl acetate), followed by a rinse in ZMD-B (methyl isobutylketone, 89%; isopropyl alcohol, 11%). The deposition of a bimetallic layer of 2 nm Cr followed by 40 nm Au was performed by sputtering of Cr and Au targets, respectively, in an ultra-high vacuum helicon sputter (MPS-4000, ULVAC Technologies Inc., Japan). The lift-off of the unwanted bimetallic layer and the removal of undeveloped resist were carried out in acetone and ZDMAC (dimethylacetamide), respectively, with strong ultra-sonication.

For large patterns, the reference and counter electrodes and the bonding pads for connection with an external electrochemical apparatus were fabricated by the combination of UV photolithography and lift-off according to the following procedure: spin-coating of a positive photo-resist (OFPR-5000, Tokyo Ohka Kogyo Co., Ltd., Tokyo, Japan), exposure to UV light, development, deposition of a bimetallic layer by sputtering, lift-off of bimetallic layer, and removal of undeveloped resist. The insulating layer with an open working window (Fig. 1b) was fabricated by standard photolithography using a 1.5- μ m-thick negative photo-resist SU8-2002 (MicroChem Inc.).

Measurements of optical properties

Electrode surfaces were characterized by a field-emission scanning electron microscope (FE-SEM, JSM-6700FT, JEOL) with a resolution of 1 nm. A photo multi-analyzer (PMA-11, Hamamatsu Photonics K. K., Shizuoka, Japan) was used to record optical extinction spectra of the nanostructured electrode surface. Finite difference time domain (FDTD) modeling was carried out using a commercial FDTD program (Lumerical, Inc.) for modeling three-dimensional field enhancement effects due to localized surface plasmons. In modeling, the x is assigned to the horizontal axis, y , vertical and z , perpendicular to both x - and y -axes. Calculations were performed on a

non-uniform rectangular grid having a minimum discretization step of $\Delta x = \Delta y = 0.5$ nm and $\Delta z = 2$ nm smaller than the narrowest nanogaps defined on the electrodes. Periodic boundary conditions were imposed at the xz and yz boundaries with a perfectly-matched layer (PML) boundary condition at the xy boundaries. The footprints of the gold nano-patterns were considered identical, with the height of 40 nm, as determined by SEM observation. The patterns were defined on a glass substrate with a refractive index of $n = 1.52$ (reported by Matsunami Glass Ltd. for the visible spectral range). The dispersion of the dielectric properties of gold was described using a Lorentz-Drude approximation (included in the Lumerical software). FDTD calculations were performed using a plane wave light source along the positive z direction from 50 nm below to the gold nano-patterns. Simulated extinction spectra and local field enhancement at different wavelengths were obtained by defining a spectrally broad (a-short-pulse) light source. Afterwards, spatial maps of the optical near-fields around the nanopatterns were extracted at the wavelength of interest.

Measurements of electrochemical SERS

The spectroelectrochemical cell for Raman scattering experiments was made by connecting the bonding edges of printed NIDAEs on a glass plate placed on an optically transparent polystyrene stage. The Cu lead wires were attached strongly to the bonding edges by Ag paste and epoxy resin adhesive. A 1×10^{-3} mol dm $^{-3}$ aqueous solution of potassium ferricyanide ($K_3[Fe(CN)_6]$) including 0.05 mol dm $^{-3}$ $KClO_4$ as base electrolyte was used for exploring both electrochemical and SERS responses to fabricated NIDAEs. Standard cyclic voltammetric measurements were performed in single (S) and generation-collection (GC) modes. In both modes RE and CE were used as a reference and counter, respectively. In the S

mode WE1 served as the working electrode, while in the GC mode, WE1 and WE2 were used as generator (G) and collector (C) electrodes, respectively (Fig. 1a). The electrochemical responses to NIDAEs were further confirmed by a three-electrode bulk system, where the three Au wires were used for reference, counter and working electrodes, respectively.

All SERS measurements were acquired with a microscope (BX51, Olympus). Light from a near-IR laser diode ($\lambda = 785$ nm) with a power of 10 mW was irradiated onto the surfaces of NIDAEs placed on the microscope stage through a 100 \times magnification water-immersion objective lens of a numerical aperture NA = 0.75 (LMPlanFL, Olympus). The SERS measurement was carried out at a slightly de-focused condition in order to avoid the damage of nano-structures due to absorption heating. SERS spectra were collected on an Acton SP300i (Princeton Instruments) imaging spectrometer equipped with a charge coupled device (CCD) camera cooled at -100°C by liquid nitrogen. Each spectrum was collected with a spectral integration time of 25 s and at spectral resolution smaller than 3 cm^{-1} . For electrochemical SERS, spectra were obtained in the S and GC modes at a steady state current using an amperometric technique. The electrode potential control during the electrochemical or *in situ* electrochemical SERS measurements was maintained using a dual potentiometer (ALS Model 832a, BAS Inc., Tokyo, Japan). All potential values were defined relative to a reference Au electrode incorporated onto an IDAE plate.

Results and Discussion

Optical properties

The design and layout of developed NIDAEs are illustrated in Fig. 1. The electrode array was made of 13 band-electrodes of Au; the dimensions of each were 120 μm -long by 10 μm -wide separated by a 1- μm space. On the smaller scale, the bands were consisted of $\sim 94 \times 94 \times 40$ nm³ Au nano-blocks, with four nano-blocks, q_i ($i = 1, 2, 3, 4$) arranged around the central nanoblock, p , along diagonals (Fig. 1e) forming a pattern consisting of five nanoblocks in total. The nanogaps were formed between p and the four neighboring q_i 's, which, in turn, were electrically interconnected with the large nanoblocks, r , into the NIDAE. The nanogaps generated between the vertexes of nanoblocks are those particular locations where local field enhancement takes place and where optical linear as well as nonlinear effects are enhanced.

The polarization-dependent experimental optical extinction, numerically simulated extinction and field-enhancement spectra are summarized in Fig. 2. Both x -/ y - and xy - (diagonal) polarized incident light give rise two dominant resonance peaks around at $\lambda_{1\text{ex}} = 580$ nm and $\lambda_{2\text{ex}} = 743$ nm in air (1 and 2, respectively, in Fig. 2a). In water, these bands are red shifted at around $\lambda_{1\text{ex}} = 595$ nm and $\lambda_{2\text{ex}} = 785$ nm due to the difference in refractive indexes between air and water. To better understand the origin of these peaks, we constructed three different FDTD models; simulation results along with the model unit are shown in Fig. 2a. Simulation using only the central nanoblock, p , shows an extinction peak at $\lambda_0 = 636$ nm (3 of Fig. 2a). The model unit without p yields two extinction peaks at around $\lambda_1 = 576$ nm and $\lambda_2 = 644$ nm (4 of Fig. 2a). The peak λ_2 is very close to λ_0 originating from the dipole resonance induced at the single nanoblock, as determined on a contour diagram of the electric field distribution extracted to the corresponding extinction peak wavelengths (Fig. 2b). The former peak, λ_1 , is a signature of the narrowest feature sizes, L (Fig. 1d), produced by the overlapping of interconnectors, r and q_i , which is unequivocally proved from the electric field contour map

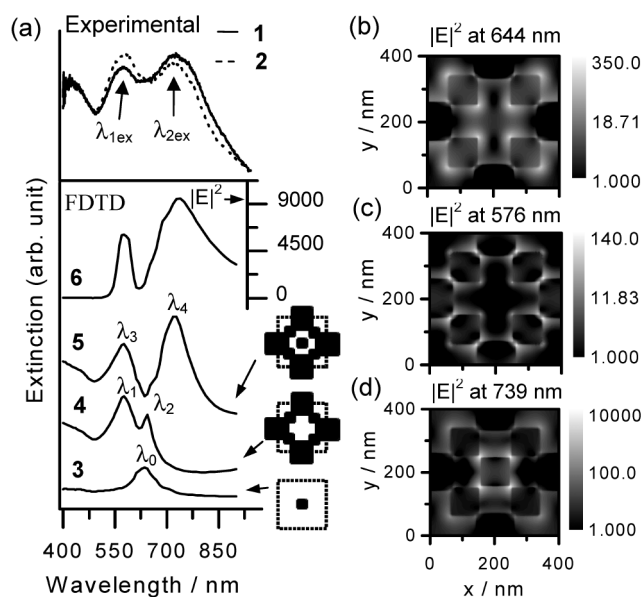


Fig. 2 (a) Optical extinction spectra: top panel experimental, 1 for x - and 2 for xy - (diagonal) polarizations; bottom panel FDTD simulation, 3 with central block, 4 without central block, 5 for model unit and 6 for electric field enhancement spectra using model unit; dotted rectangle refers to simulation area. (b) - (d) Contour maps of electric field distributions (logarithmic scale) at 644 nm and 576 nm using the model unit without the central block and at 739 nm using the model unit, respectively, relative to incident light intensity $|E|^2 = 1$.

derived at that wavelength (Fig. 2c). The model unit also shows two extinction peaks at $\lambda_3 = 578$ nm and $\lambda_4 = 739$ nm (5 of Fig. 2a). The λ_3 coincided with λ_1 , the co-positionings of the large red-shifted peak λ_4 from λ_0 with experimentally observed peaks $\lambda_{1\text{ex}}$ and $\lambda_{2\text{ex}}$ reveal the secret their origin. The peak at $\lambda_{1\text{ex}}$ is due to the narrowest feature size, L , while $\lambda_{2\text{ex}}$ derives the dipole-dipole coupling resonance through p to q_i as revealed by the contour map shown in Fig. 2d.

The assignment of $\lambda_{1\text{ex}}$ and $\lambda_{2\text{ex}}$ was confirmed by polarization-dependent extinction spectra. The xy - (diagonal) polarized incident light shows a red-shift (~ 7 nm) of $\lambda_{1\text{ex}}$ with increased extinction relative to x -/ y -polarization, while for $\lambda_{2\text{ex}}$ the peak positions are found to be invariant with reduced intensity. The red-shift in $\lambda_{1\text{ex}}$ accounts for the dipole modes in xy -polarization being larger than those in the x -/ y -directions. The oscillating behavior of intensity can be rationalized by considering dipole vectors and their x -/ y -components. The contour maps derived from FDTD simulation reveal that all dipoles induced in a single nanoblock or in narrowest features are distributed in xy - (diagonal) directions. For $\lambda_{1\text{ex}}$ both in x -/ y - and xy -polarization, the eight narrowest feature sizes are involved in resonance and it would be expected that the intensity in x -/ y -polarization can be derived as $1/\sqrt{2}$ times of that in xy -polarization. From the contour map it is seen that in the case of the $\lambda_{2\text{ex}}$ peak, xy -polarization makes use of three nanoblocks through p (q_1 - p , p - q_3 , or q_2 - p , p - q_4) for dipole-dipole coupling resonance, while all nanoblocks in the model unit (p and q_i) are engaged in coupling for the x -/ y -polarization. The extinction intensity ratio of xy - to x -/ y -polarization can be estimated as $3:5/\sqrt{2}$, or 3:3.5. The assumption adopted here explains the experimental extinction intensity and oscillation behavior semi-quantitatively, because the theoretical calculations were performed using the ideal shape of nanoblocks, while the diagonal lengths of the real nanoblocks are slightly smaller than

those of the theoretical one. Invariance in peak positions is attributed to the same effective dipole length produced by dipole-dipole coupling in xy - and x -/ y -polarizations, since in both cases dipole-dipole coupling takes place through p to q_i .

The spectral shape and position of both resonances were found to depend on the nanogap width, periodicity and each nanoblock's dimensions, as one would expect. Indeed, the overall length of the nanoparticles and their connectivity *via* the evanescent field determines the structural length, and hence the spectral position of the extinction peak. Small nanogaps are potentially important because localized surface plasmon modes are predominantly localized in the nanogaps and the electrical field is strongly enhanced at the gaps. For a better understanding, field enhancement spectra, which are the squares of the amplitudes of the electric fields, were also calculated by FDTD modeling. The field monitor placed at the top of gold surface was used to calculate field enhancement using the equation: $|E|^2 = |E_x|^2 + |E_y|^2 + |E_z|^2$. This is shown in **6** of Fig. 2a along with the calculated extinction spectra. The electric field distribution map (Fig. 2d) explicitly shows localization sites at nano-gaps, where enhancement of the electric field reaches 10^4 . Similar field distributions and enhancement have been observed on simpler symmetrical checker board gold nanopatterns.^{25,27}

The electrochemical SERS activity

The measured cyclic voltammograms of 1×10^{-3} mol dm⁻³ of $K_3[Fe(CN)_6]$ in 0.05 mol dm⁻³ $KClO_4$ performed in S and GC modes using NIDAEs and the three-electrode bulk system at a potential sweep rate of 20 mV s⁻¹ are summarized in Fig. 3a. Within the selected potential region (where the anodic peak for Au-oxide formation, or the cathodic peak for stripping of such oxides was not observed; inset 4, Fig. 3a), $K_3[Fe(CN)_6]$ shows a peak-shaped cyclic voltammogram with a reduction peak at -0.169 V and an oxidation peak at -0.099 V in the bulk electrode system (inset 5, Fig. 3a), while for NIDAEs the cyclic voltammogram became sigmoidal in shape in both modes due to reaction-rate limited redox events. The calculated redox cycling number, RC, which is the ratio of the limiting current in GC mode to that of S mode, was determined to be ~ 5 ; the collection efficiency, $\sigma\%$ *i.e.*, the ratio of the limiting current at the collector electrode to that at the generator electrode was found to be $\sim 63\%$.

Normal Raman and SERS spectra were acquired by dispersing a drop of $K_3[Fe(CN)_6]$ solutions over glass and NIDAEs and irradiating with a 785-nm laser source with a typical power of 10 mW for a 25-s integration time. The Raman spectra for 1 mol dm⁻³ on glass and SERS for 1×10^{-3} mol dm⁻³ on NIDAEs are shown in Fig. 3b. The solution phase of $K_3[Fe(CN)_6]$ shows a strong band at 2126 cm⁻¹ with a broad shoulder at 2120 cm⁻¹. The band position and shape are very similar to that described in the literature^{28,29} and were assigned to a C \equiv N stretching mode. At the surface of the NIDAE, an intense peak at 2155 cm⁻¹ and a relatively broad peak at 2075 cm⁻¹ along with the multiple weaker peaks (1913, 1949, 2040, 2095, 2113, 2189 and 2266 cm⁻¹) appeared in the SERS spectra, while the bands for solution species remained. According to Korzeniewski and his co-workers,³⁰ a hexacyanoferrate(III) ion is attached to the surface *via* two cyanide ligands. With this configuration, the ion loses its structural symmetry, giving rise to additional bands as shoulders. Owing to the rapid fall-off of the enhancement mechanism with distance from the surface of the electrode, the C \equiv N stretch region is dominated by those ligands in contact with the electrode surface, and thus the peak observed at 2155 cm⁻¹ is assigned to the C \equiv N stretching mode of ligands adsorbed to the

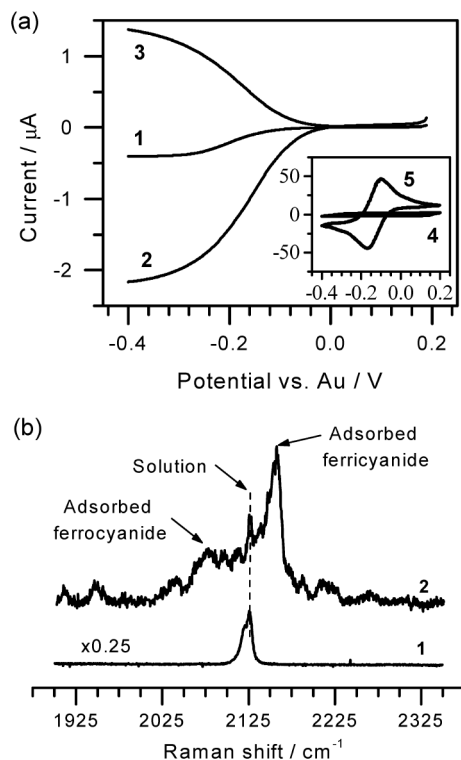


Fig. 3 (a) Cyclic voltammograms of 1×10^{-3} mol dm⁻³ $K_3[Fe(CN)_6]$ in 0.05 mol dm⁻³ $KClO_4$ observed by NIDAEs; **1** in S mode, **2** and **3** respectively, at G and C electrodes (potential kept at 0.2 V) in GC mode; potential scan rate, 20 mV s⁻¹; inset at bulk electrode, **4** in 0.05 mol dm⁻³ $KClO_4$ and **5** 1×10^{-3} mol dm⁻³ $K_3[Fe(CN)_6]$ + 0.05 mol dm⁻³ $KClO_4$, (b) Normal Raman and SERS spectra of $K_3[Fe(CN)_6]$; **1** for 1 mol dm⁻³ on glass and **2** for 1×10^{-3} mol dm⁻³ on NIDAEs.

Au surface. One would expect the stretching frequency of -CN ligand in hexacyanoferrate(II) to be shifted to lower frequency due to the less positive charge of the central Fe atom; the peak at 2075 cm⁻¹ can be assigned to the C \equiv N stretching mode of ligands in hexacyanoferrate(II) adsorbed to the Au surface. The weaker peaks at 2040, 2095, 2113, 2189 cm⁻¹ may be attributed to electron donations from the π^* orbital of the cyanide group to the metal surface³¹ and also to a bridging bond to the surface formed by the nitrogen lone pair (σ orbital), as proposed by Allen and Van Duyne.³² The other weaker peaks may be attributed to contaminations. These peaks are unaffected by changes in the bulk solution; bands due to these ligands, which are not in contact with the surface but in contact with the solution are not swamped, and information relating to the effect of ion-pair formation is preserved. The detection of a new peak with high intensity demonstrates that the light field enhancement at the nanogaps strongly facilitates SERS detection of low-concentration ions on the fabricated NIDAEs.

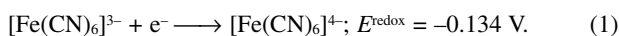
The redox cycling dependent of SERS

For a detailed investigation of the redox cycling dependence on SERS signals, SERS spectra of $K_3[Fe(CN)_6]$ were recorded against the applied potential at a steady current obtained by the amperometric technique in both S and GC modes. In both modes, the potential of the WE1 electrode was varied by 0.05 V in each step within the 0.2 to -0.4 V potential region, while the potential of the WE2 electrode was kept at 0.2 V. Figure 4a represents the potential dependent SERS spectra of 1×10^{-3} mol dm⁻³ of $K_3[Fe(CN)_6]$ in 0.05 mol dm⁻³ $KClO_4$ in

both S and GC modes.

SERS at the electrode causes secondary effects, such as adsorption, desorption, and electrochemical reactions of the pre-surface species. It is well-known that high-light intensity fields attract and dipole-orient optically polarized molecules.^{33,34} In both S and GC modes, SERS bands appearing at 2155 cm⁻¹ showed similar potential-dependent behavior except for the magnitude of intensity. In the single mode, the band intensity started to decrease (first panel, Fig. 4a) as the potential shifted to the negative direction, and at the negative end of the studied potential range it reached ~14% of initial potential, while in GC mode it was about to ~70%.

The area of the 2155 cm⁻¹ band was calculated for obtaining a correlation between electrical current and SERS signals; the redox cycling number and collection efficiency come from measured current values and SERS signals. Figure 4b summarizes the potential dependency of the current, the SERS signals, redox cycling (RC) number and collection efficiency, $\sigma\%$. As we see from **1** and **2** of Fig. 4b, the reduction currents and SERS signals have a sigmoidal curve shape as a function of applied potential with a great sensitivity within the potential range between -0.05 to -0.2 V. This sensitivity is a consequence of the reduction of [Fe(CN)₆]³⁻ ions *via* one electron according to the following reaction:



The area of 2075 cm⁻¹ band was found to be increased as the potential shifted to negative direction, and this band has been assigned²⁹ to the product, [Fe(CN)₆]⁴⁻ ions.

The sensitivities of the reduction current and SERS signals to potential within the above mentioned range exhibited counter behaviors to each other in S and GC mode experiments. This result is reasonable, and can be rationalized by considering the relative amounts of species present at the electrode surface, the volume of the diffusion layer, redox cycling and feedback effects. In the S mode, as the band area of the [Fe(CN)₆]⁴⁻ ions against the negative sweep of the applied potential increased, the reaction (1) proceeds with the increasing concentration of [Fe(CN)₆]⁴⁻ ions at or very close to the electrode surface, and the rate of this reaction to the negative potential decreased due to the partial occupation of surface sites by reduced product and the continuous growing of the diffusion layer. Since in this scenario the concentration of [Fe(CN)₆]³⁻ ions at the interface is declining, and the SERS band intensity due to [Fe(CN)₆]³⁻ ions decreases to ~14% of that of the initial potential. On the other hand, in the GC mode experiment, the C electrode kept at 0.2 V triggers the diffusion of reduced product from the vicinity of the G electrode and finally oxidizes to the original one according to the reaction:



The triggered diffusion of [Fe(CN)₆]⁴⁻ from the G electrode and the feedback reaction (2) taking place at the C electrode cause the volume of the diffusion layer around the G electrode to be very small. The surface concentration of [Fe(CN)₆]³⁻ ion is significantly increased; hence, the high reduction rate and reduction current in the GC mode can be explained. Due to the same effects, the SERS signals for [Fe(CN)₆]³⁻ ions are amplified relative to the S mode as the potential shifted to the negative direction from -0.05 V. Note that the SERS band area of [Fe(CN)₆]³⁻ ions at the negative end of applied potential in the S mode was estimated to be ~14% of initial potential. The standard error of this estimation was quite large because of the

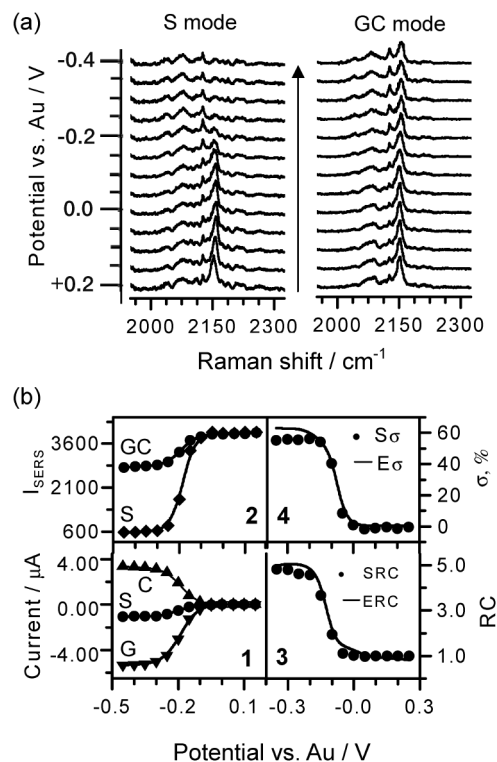


Fig. 4 (a) Potential dependent SERS spectra of $1 \times 10^{-3} \text{ mol dm}^{-3} \text{ K}_3[\text{Fe}(\text{CN})_6]$: first panel for S mode and second for GC mode, (b) Variation of redox currents **1**, SERS **2**, redox cycling number **3** (ERC calculated from redox current and SRC from SERS) and collection efficiency **4** ($E\sigma$ from redox current and $S\sigma$ from SERS) as a function of potential; for S, G, C, GC see text in details.

very weak SERS band at this potential (top spectra of first panel in Fig. 4a), while in the GC mode at the same potential, the intensity of the SERS band was comparable to that observed at the initial potential. So, the use of SERS-functionality NIDAEs not only improves the analytical sensitivity but also the detection qualities of analytical techniques.

The redox cycling number, RC, and the collection efficiency, $\sigma\%$ lend further insight into the redox cycling and feedback phenomena. The RC number and σ calculated from electrochemical currents and SERS signals are shown in **3** and **4** of Fig. 4b, respectively. The SERS collection efficiencies ($S\sigma$) were calculated from the differences of percent of SERS signals relative to the value at the initial potential between GC and S modes. In Fig. 4b, **3** clearly reveals that at the limiting region the electrochemical redox cycling (ERC) reaches a value of 4.97 and that the SERS redox cycling (SRC) numbers are in good agreement with each other. This demonstrates that SERS signals in the GC-mode experiment were amplified by the electrochemical redox cycling number. It is apparent from **4** of Fig. 4b that the electrochemical collection efficiency ($E\sigma$) and $S\sigma$ are also well correlated. The strong correlation between those parameters derived from the redox currents and the SERS signals indicates that the nanostructured NIDAEs with SERS functionality are promising for *in situ* quantitative and qualitative analyses.

SERS spectra measured at different redox potentials can be linked to the conformational changes of molecules on the surface and can be used to follow adsorption-desorption dynamics in time and to determine the lifetime of intermediate redox products. Redox cycling can be used to enhance the

SERS signal that might have been caused by different mechanisms depending on the materials, *e.g.*, molecules in the high-intensity region can be affected by heating and their vibrational spectrum can be altered by thermal damage; however, redox cycling can help to recover/replace them by release and recapture at the hot-spots. Further systematic studies are planned to establish gap-size dependences and to test different redox species using similar SERS-NIDAEs designs.

Conclusions

Au-NIDAEs were fabricated successfully using high precision electron beam lithography. The electric field enhancement at nanogaps achieved by FDTD simulation revealed promising applications in manipulating nonlinear optical events. Its small size is in high demand for integration with miniaturized devices and technologies, such as lab-on-a-chip systems, μ -TAS, MEMS, microfluidics, and so on. The electrodes were used to investigate the electrochemical SERS responses of $[\text{Fe}(\text{CN})_6]^{3-}$ ions. Electrochemical and SERS experiments were carried out in S and GC modes. In single mode, the estimated area of the 2155 cm^{-1} band was found to be reduced to near zero, while in GC mode it was strong over the entire studied potential region reflecting that SERS-functionality NIDAEs offer a new opportunity in analytical science to improve analytical sensitivity and detection capability. The parameters such as redox cycling number and collection efficiency derived from electrochemical currents and SERS signals were observed to be well correlated, which is evidence of the technique's potential for quantitative applications.

We have also used fabricated NIDAEs of similar design for collecting electrochemical SERS responses of irreversible electroactive species, namely, crystal violet molecules in aqueous KCl/KClO₄ solutions. Redox cycling or feedback effects were found to be operative when the inter-electrode band separation was smaller. The details of this study will be summarized in a future article.

Acknowledgements

This work was supported by funding from the Ministry of Education, Culture, Sports, Science, and Technology of Japan: KAKENHI Grant-in-Aid for Scientific Research on the Priority Area "Strong Photon-Molecule Coupling Fields" (No. 470 (No. 19049001)) and 20710068, Grants-in-Aid from Hokkaido Innovation through Nanotechnology Support (HINTS), Monbukagakusho Scholarship for foreign students support, and Global Center of Excellence (GCOE) through Graduate School of Information Science and Technology, Hokkaido University, Japan.

References

- D. G. Sanderson and L. B. Anderson, *Anal. Chem.*, **1985**, *57*, 2388.
- (a) O. Niwa, M. Morita, and H. Tabei, *Electroanalysis*, **1991**, *3*, 163; (b) O. Niwa, M. Morita, and H. Tabei, *Anal. Chem.*, **1990**, *62*, 447; (c) O. Niwa, M. Morita, and H. Tabei, *J. Electroanal. Chem.*, **1989**, *267*, 291.
- (a) H. Tabei, M. Takahashi, S. Hoshino, O. Niwa, and T. Horiuchi, *Anal. Chem.*, **1994**, *66*, 3500; (b) H. Tabei, T. Horiuchi, O. Niwa, and M. Morita, *J. Electroanal. Chem.*, **1992**, *326*, 339; (c) H. Tabei, M. Morita, O. Niwa, and T. Horiuchi, *J. Electroanal. Chem.*, **1992**, *334*, 25.
- M. Takahashi, M. Morita, O. Niwa, and H. Tabei, *J. Electroanal. Chem.*, **1992**, *335*, 253.
- (a) T. Horiuchi, O. Niwa, M. Morita, and H. Tabei, *Anal. Chem.*, **1992**, *64*, 3206; (b) T. Horiuchi, O. Niwa, M. Morita, and H. Tabei, *J. Electrochem. Soc.*, **1991**, *138*, 3549; (c) T. Horiuchi, O. Niwa, M. Morita, and H. Tabei, *J. Electroanal. Chem.*, **1990**, *295*, 25.
- C. S. Henry and I. Fritsch, *J. Electrochem. Soc.*, **1999**, *143*, 3367.
- M. Morita, O. Niwa, and T. Horiuchi, *Electrochim. Acta*, **1997**, *42*, 3177.
- W. R. Vandaveer, D. J. Woodward, and I. Fritsch, *Electrochim. Acta*, **2003**, *48*, 3341.
- E. Nebling, T. Grunwald, J. Albers, P. Schäfer, and R. Hintsche, *Anal. Chem.*, **2004**, *76*, 689.
- Z. Liu, O. Niwa, R. Kurita, and T. Horiuchi, *Anal. Chem.*, **2000**, *72*, 1315.
- A. J. Bard, F. R. F. Fan, J. Kwak, and O. Lev, *Anal. Chem.*, **1989**, *61*, 132.
- K. Aoki, M. Morita, O. Niwa, and H. Tabei, *J. Electroanal. Chem.*, **1988**, *256*, 269.
- L. Malaquin, C. Vieu, C. Martinez, B. Steck, and F. Carcenac, *Nanotechnology*, **2005**, *16*, S240.
- A. J. Bard, J. A. Crayston, G. P. Kittleson, T. V. Shea, and M. S. Wrighton, *Anal. Chem.*, **1986**, *58*, 2321.
- U. Wollenberger, M. Paeschke, and R. Hintsche, *Analyst*, **1994**, *119*, 1245.
- E. D. Goluch, B. Wolfrum, P. S. Singh, M. A. G. Zevenbergen, and S. G. Lemay, *Anal. Bioanal. Chem.*, **2009**, *394*, 447.
- A. J. Bard and L. R. Faulkner, in "Electrochemical Methods: Fundamentals and Applications", 2nd ed., **2001**, Chap. 6, John Wiley & Sons, Inc., 243.
- W. Kaim and A. Klein, "Spectroelectrochemistry", **2008**, The Royal Society of Chemistry, Cambridge.
- D. L. Jeanmaire and R. P. Van Duyne, *J. Electroanal. Chem.*, **1977**, *84*, 1.
- L. A. Dick, A. D. McFarland, C. L. Haynes, and R. P. Van Duyne, *J. Phys. Chem. B*, **2002**, *106*, 853.
- Z.-Q. Tian, B. Ren, and D.-Y. Wu, *J. Phys. Chem. B*, **2002**, *106*, 9463.
- N. Ohta and I. Yagi, *J. Phys. Chem. C*, **2008**, *112*, 17603.
- T.-H. Lin, N. C. Linn, L. Tarajano, B. Jiang, and P. Jiang, *J. Phys. Chem. C*, **2009**, *113*, 1367.
- M. E. Abdelsalam, P. N. Bartlett, J. J. Baumberg, S. Cintra, T. A. Kelf, and A. E. Russell, *Electrochem. Commun.*, **2005**, *7*, 740.
- K. Ueno, V. Mizeikis, S. Juodkazis, K. Sasaki, and H. Misawa, *Opt. Lett.*, **2005**, *30*, 2158.
- K. Ueno, S. Juodkazis, T. Shibuya, Y. Yokota, V. Mizeikis, K. Sasaki, and H. Misawa, *J. Am. Chem. Soc.*, **2008**, *130*, 6928.
- K. Ueno, S. Juodkazis, V. Mizeikis, K. Sasaki, and H. Misawa, *Adv. Mater.*, **2008**, *20*, 26.
- W. P. Griffith and G. T. Turner, *J. Chem. Soc. A*, **1970**, 858.
- R. B. Lowry, *J. Raman Spectrosc.*, **1991**, *22*, 805.
- C. Korzeniewski, M. W. Severson, P. P. Schmidt, S. Pons, and M. Fleischmann, *J. Phys. Chem.*, **1987**, *91*, 5568.
- S. Pons, M. Datta, J. F. McAleer, and A. S. Hinman, *J. Electroanal. Chem.*, **1984**, *160*, 369.
- C. S. Allen and R. P. Van Duyne, *J. Am. Chem. Soc.*, **1981**, *103*, 7497.
- K. Murakoshi, H. Tanaka, Y. Sawai, and Y. Nakato, *J. Phys. Chem. B*, **2002**, *106*, 3041.
- Y. Nabetani, H. Yoshikawa, A. C. Grimsdale, K. Mullen, and H. Masuhara, *Langmuir*, **2007**, *23*, 6725.